remote sensing

MDPI

Article

Fusing Instantaneous and Historical Spatial–Contextual Brightness Temperature Differences for Himawari-8/9 Active Fire Detection

Xirong Liu and Yanfang Ming *

College of Geodesy and Geomatics, Shandong University of Science and Technology, Qingdao 266590, China; liuxirong@sdust.edu.cn

* Correspondence: myf@sdust.edu.cn

Highlights

What are the main findings?

- A dual-feature algorithm is proposed to decouple fire-induced anomalies from inherent surface thermal heterogeneity by fusing instantaneous and historical spatial–contextual differences.
- Validation against over 55,000 verified fire pixels yields a commission error of 2.9% and an F1-score of 0.76, representing a 38.2% relative improvement over the operational WLF product.
- A stratified sub-pixel assessment quantifies the algorithm's detection boundaries and its superior sensitivity to small-scale fires.

What are the implications of the main findings?

- Enhanced sensitivity to low-temperature, smoke-obscured, and early-stage fires confirms the algorithm's effectiveness for hazard mitigation in complex environmental scenarios.
- Full-disk processing in less than one minute and a transferable framework provide a robust technical basis for establishing a globally coordinated fire monitoring system.

Abstract

Efficient and accurate active fire detection is crucial for timely firefighting and mitigating hazards. Geostationary satellites deliver high-frequency observations that offer valuable data for near-real-time fire monitoring. However, current operational fire detection algorithms often underutilize temporal information, failing to decouple fire-induced anomalies from inherent surface thermal heterogeneity, which results in frequent false alarms. To address this limitation, we constructed a ten-day historical background brightness temperature (BT) reference database from multi-year Himawari-8/9 data, serving as a stable, fire-undisturbed baseline. Based on this, an active fire detection algorithm was developed that integrates instantaneous spatial–contextual differences with historical deviations of these differences from the reference database. Evaluated against a robust dataset of over 55,000 fire pixels (cross-verified using 10 m Sentinel-2 burn-scar data), the proposed algorithm significantly outperforms the Himawari-8/9 Wildfire (WLF) product, achieving a commission error (CE) of 2.9%, an omission error (OE) of 37.5%, and an F1-score of 0.76. The framework demonstrated superior detection accuracy in challenging scenarios such as low-temperature, smoke-obscured, and early-stage fires, while maintained robust performance across diverse fire types. The approach enables rapid full-disk fire detection in less than one minute and can be adapted to other geostationary satellites, providing a technical foundation for building a globally coordinated fire monitoring system.

Check for updates

Academic Editor: Eriita Jones

Received: 3 February 2026
Revised: 6 March 2026
Accepted: 10 March 2026
Published: 16 March 2026

Copyright: © 2026 by the authors. Licensee MDPI, Basel, Switzerland. This article is an open access article distributed under the terms and conditions of the Creative Commons Attribution (CC BY) license.

Keywords: active fire detection; Himawari-8/9; historical background reference database; instantaneous spatial–contextual difference; deviations from historical reference

1. Introduction

As one of the most prevalent and destructive natural disasters, wildfires exert profound and far-reaching impacts on Earth's ecosystems and human societies [1,2]. Beyond immediate damage to vegetation and infrastructure, wildfires release vast quantities of greenhouse gases and aerosols (e.g., $PM_{2.5}$ and black carbon), degrading air quality, threatening public health, and disrupting the global climate system [3–7]. Driven by climate warming and intensified human activities, the frequency, intensity, and scale of global wildfires have shown a marked increasing trend in recent years [8,9]. Consequently, the development of timely and accurate active fire detection technologies is paramount for effective fire prevention and disaster risk reduction.

Satellite remote sensing has become a cornerstone of active fire monitoring, offering advantages in spatial coverage, multi-spectral capabilities and cost-effectiveness over traditional methods (e.g., watchtowers, video surveillance) [10,11]. While polar-orbiting satellites (e.g., MODIS, VIIRS) have been widely used, their low temporal resolution (typically 2–6 overpasses per day) often results in missed detections of short-lived fires and fails to capture critical fire progression dynamics [8,12–14]. In contrast, the new generation of geostationary satellites, such as Himawari-8/9, provides continuous observation at intervals as short as 10 min. This high-frequency observation capability is indispensable for early fire monitoring and tracking fire spread, making it a critical tool for achieving truly timely fire management [13,15,16].

Operational active fire detection algorithms for satellites predominantly rely on monophase threshold-based methods that identify thermal anomalies by comparing a target pixel's brightness temperature (BT) in mid-wave infrared (MIR, ~4 μm) and thermal infrared (TIR, ~11 μm) channels against its immediate spatial background [6,12,15]. This method offers the distinct advantage of high sensitivity to localized thermal anomalies and requires only single-scene processing, making it computationally straightforward and widely adopted. However, this reliance on a single instantaneous spatial–contextual analysis disregards temporal information (specifically the predictable diurnal thermal behavior of land surfaces) and is vulnerable to spatial heterogeneity. Physically, different land cover types possess distinct thermal inertias. In highly heterogeneous regions (e.g., vegetation-bare soil boundaries or urban heat islands), these inertia differences lead to persistent, inherent spatial temperature gradients during the diurnal heating cycle. Instantaneous algorithms frequently misinterpret these static background contrasts as active fires, leading to frequent false alarms [17–24]. For geostationary satellites, this issue is exacerbated by high observation frequency, resulting in accumulated commission errors—illustrated by the Himawari-8/9 Wildfire (WLF) product over China, which generated nearly 13,000 false alarms monthly [10].

To address these false alarms, recent advancements in active fire detection have increasingly integrated temporal information. These existing spatio-temporal approaches typically function as dynamic change detection algorithms, which identify fires by calculating the temporal derivative of the MIR BT (i.e., comparing the current $BT_7(t)$ with the previous time slot $BT_7(t-1)$) [25–27]. By tracking temporal variations, these methods offer the advantage of effectively suppressing static spatial false alarms (e.g., permanent bare soil edges) and are highly effective for capturing rapid fire ignitions where the thermal signal changes abruptly. While effective in these specific scenarios, these methods suffer

from two fundamental limitations. First, during sustained burning or a fire's waning stage, the temporal difference in MIR BT changes little or may even become negative, resulting in missed detections [25]. Second, they are prone to misclassifying non-fire normal overheated conditions, such as particularly hot weather or rapid diurnal surface heating, as fire events [24]. In such scenarios, the rapid temporal rise in surface temperature mimics the thermal signature of a fire ignition, leading to false alarms. Furthermore, a single previous observation is highly vulnerable to cloud contamination and lacks a stable historical baseline, and constructing reliable, cloud- and fire-free references for each pixel in near-real-time (NRT) remains computationally prohibitive for full-disk processing. Essentially, existing methods have focused on the temporal difference of absolute BT but have largely overlooked the temporal stability of spatial–contextual differences.

To bridge this gap, this study proposes a dual-feature active fire detection algorithm that systematically integrates instantaneous spatial–contextual differences with deviations from a historical background baseline. The theoretical basis of this integration is that while absolute temperatures vary with weather, the spatial thermal contrast between a target pixel and its background remains relatively stable over time for non-fire surfaces (representing the inherent surface heterogeneity). Unlike existing dynamic change detection methods that track the temporal change of MIR BT, our approach requires the thermal anomaly to exhibit both a pronounced instantaneous spatial contrast and a significant deviation from its historical spatial norm. This dual-feature integration effectively decouples fire-induced anomalies from both weather-induced absolute heating and static landscape heterogeneity. This design achieves two key innovations: (1) a comprehensive, cloud- and fire-free reference database was constructed from multi-year Himawari-8/9 observations, establishing a stable and representative background baseline; (2) we effectively combined instantaneous and historical spatial–contextual BT difference features, maintaining high sensitivity to active fires while achieving robust false-alarm suppression. By advancing toward truly operational geostationary satellite active fire monitoring, this work aims to enhance the accuracy, reliability, and timeliness of global wildfire surveillance.

The structure of this study is organized as follows: Section 2 details the data employed in this study. Section 3 comprehensively describes the implementation process of proposed algorithm, and evaluation metrics. Section 4 presents experimental results, overall quantitative validation, and an in-depth examination of algorithmic boundaries. Section 5 discusses the robustness of the historical baseline, along with the primary performance drivers and physical limitations of the proposed algorithm. Finally, Section 6 synthesizes the principal conclusion and suggests directions for future research.

2. Materials

2.1. Himawari-8/9 Satellite Data

The Himawari-8 and Himawari-9 satellites, launched by the Japan Meteorological Agency (JMA) in October 2014 and November 2016 respectively, represent a new generation of geostationary systems with enhanced observational capabilities [28,29]. They are equipped with the Advanced Himawari Imager (AHI), a 16-channel multispectral sensor covering a wavelength range from 0.45 to 13.3 μm. The AHI delivers full-disk observations of the hemisphere encompassing Australia and East Asia (60°S–60°N, 80°E–160°W) at a 10-min temporal resolution [30,31]. The improved spatial resolution (2 km at nadir) and radiometric resolution in the infrared bands, specifically bands 7 and 14 used in this study, enables superior active fire detection capabilities compared to prior geostationary systems [17,23].

2.2. Validation Data

2.2.1. Himawari-8/9 Wildfire Product

The official Himawari-8/9 WLF Level2 product, released by Japan Aerospace Exploration Agency (JAXA) in CSV format, was used for comparison with the performance of proposed approach. This product offers fire-related data including geolocation, fire radiative power (FRP), and reliability (low, normal, and high) [8,32,33]. The operational WLF algorithm adopts a threshold-based approach, which identifies fires based on the normalized deviation of the BT at 3.9 μm from the background temperature derived from the 10.8 μm channel in an 11 × 11 pixels window (https://www.eorc.jaxa.jp/ptree/documents/README_Himawari_L2WLF.txt, accessed on 1 February 2026).

2.2.2. VIIRS Active Fire Product

The VIIRS active fire product (VNP14IMG and VJ114IMG) was employed as reference data to evaluate the performance of our proposed algorithm. With a spatial resolution of 375 m and approximately four overpasses per day, this product reports detection time, location (latitude and longitude), confidence (low, nominal, and high), FRP, and BT at the 4 μm and 11 μm bands [14,34]. The VIIRS fire product algorithm was built upon the heritage MODIS active fire detection algorithm but incorporates several modifications to accommodate the unique characteristics of the 375 m VIIRS imagery. Owing to its finer spatial resolution, the VIIRS product exhibits markedly higher sensitivity to relatively small fires and offers more precise mapping of large fire perimeters. Consequently, it has been widely adopted as a validation reference in active fire detection studies [8,32,35,36].

To ensure the reliability of this reference data, a stringent validation procedure was implemented. First, only nominal and high confidence level VIIRS active fire detections were selected. Subsequently, their authenticity was verified using the differenced Normalized Burn Ratio (dNBR) computed from pre- and post-fire Sentinel-2 imagery [37–39]. A VIIRS fire pixel was designated as a confirmed true fire only when the high-resolution Sentinel-2 pixels within its footprint exhibited burn scars (dNBR $\geq$ 0.2). Otherwise, it was discarded as a false alarm.

Figure 1 presents the validation of VIIRS active fire products using Sentinel-2 derived burn scars. In the first-row example from 18 April 2024, the dNBR successfully extracted distinct burn scars from an agricultural fire, thereby confirming the reliability of the fire event. In contrast, the case from 13 March 2024 (second row) revealed a false alarm reported by VIIRS at a bare soil–vegetation boundary. The dNBR analysis over this region showed no detectable burn scar, enabling the effective exclusion of this false positive. These results demonstrate that validation with high-spatial-resolution burn scar data can enhance the accuracy assessment of medium-resolution fire products and improve the reliability of fire reference datasets.

The performance of the proposed algorithm was evaluated using 40 days of data from different seasons in 2023 (mid-January, April, July, and October). During this period, 55,561 verified VIIRS fires—encompassing multiple types, including forest, agricultural, and grassland fires—were detected across the Himawari-8/9 full-disk. The spatial distribution of these fires is shown in Figure 2.

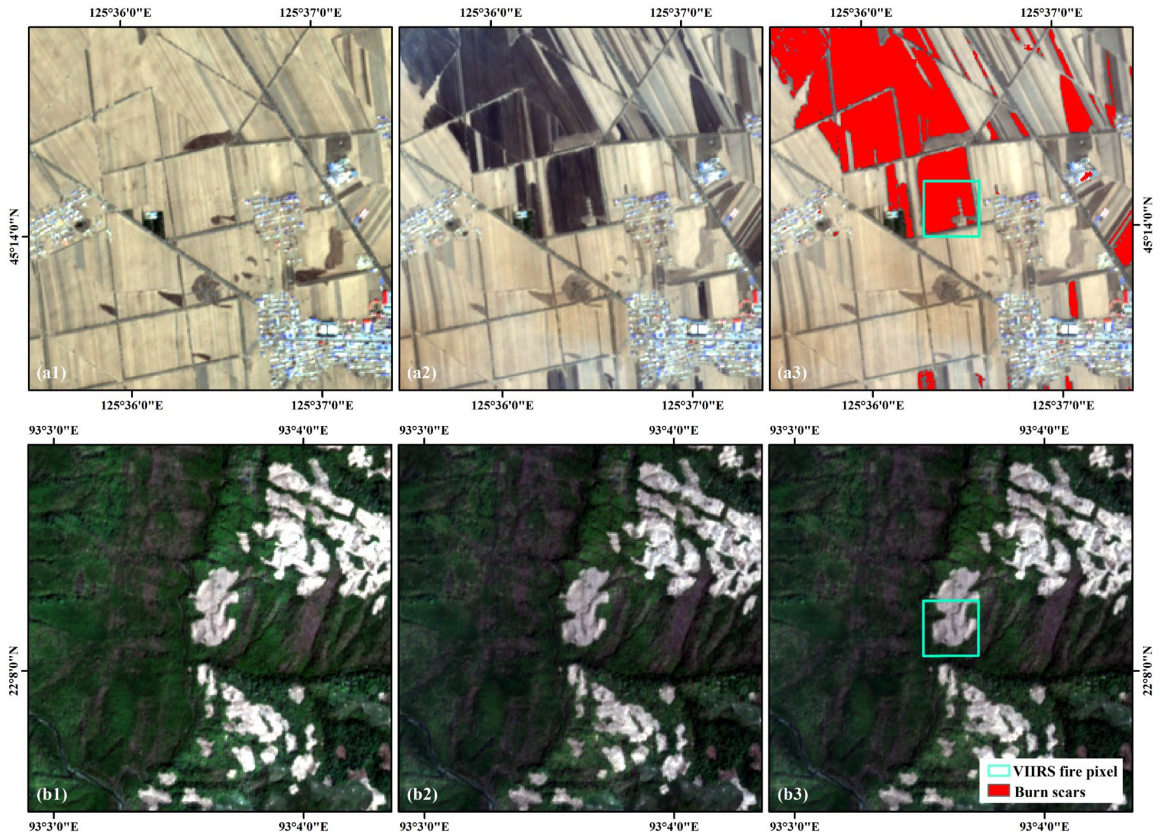


Figure 1. Validation of VIIRS active fire detections using Sentinel-2 derived burnt areas. (**a1**,**b1**) represent the pre-fire Sentinel-2 imagery; (**a2**,**b2**) represent the post-fire Sentinel-2 imagery; (**a3**,**b3**) represent the corresponding burn scars within the VIIRS fire pixel footprint, respectively.

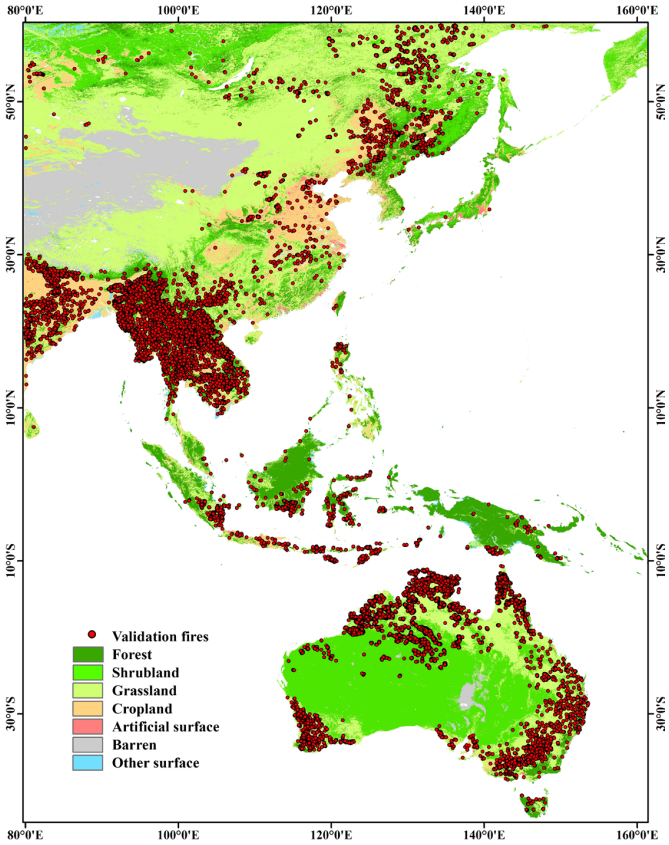


Figure 2. Geographic distribution of VIIRS active fires for algorithm validation.

3. Methods

3.1. Historical Background Reference Database Construction

The historical background reference database was established to serve as a fire-undisturbed baseline, characterizing the normal thermal radiation signal of the land surface and atmosphere under non-fire conditions. Furthermore, the database incorporated the inherent natural variability of signals across both spatial and temporal dimensions (here referring to normal fluctuations unrelated to fire) [40,41]. During its construction, reference images were selected to be as homogeneous as possible with the target imagery in terms of time phase, season, and geographical context. To more effectively mitigate the influence of dynamic factors like atmospheric conditions and vegetation phenology, this study constructed a ten-day background reference database. For each specific observation time slot of day, data from the same month and the same ten-day period across four years (2021–2024) were used to establish the database. The 4-year period was selected to provide a balance between ensuring sufficient cloud-free samples in persistently cloudy regions and maintaining the representativeness of the current land cover state.

The resulting database comprises four statistical layers: the mean BT of band 7, the mean BT of band 14, and their corresponding standard deviations. Within this framework, the mean values represent the expected BT under stable, fire-free background conditions, while the standard deviation reflects unpredictable signal variations induced by surface and atmospheric conditions (e.g., changes in soil moisture and atmospheric humidity), representing the level of residual noise [24,42]. Importantly, calculating these statistics over a multi-year period allows the standard deviation to encompass general interannual meteorological variations, providing a robust statistical buffer against typical climate fluctuations. To ensure the statistical reliability of these layers, a minimum threshold of three valid cloud-free observations over the 4-year period was required ($N \geq 3$). The choice of the 10-day window was justified by a comparative analysis of different temporal scales (7, 10, and 15 days). Quantitatively, as the window narrows to 7 days, the percentage of invalid pixels in the database (those failing to meet the $N \geq 3$ requirement) increases to 6.2%, causing significant data gaps. Conversely, extending the window to 15 days introduces excessive phenological noise. For instance, in seasonally dynamic regions like the croplands of Shandong, China, the historical standard deviation (σ) of band 7 in July increases from 0.88 K (10-day) to 1.45 K (15-day) due to crop harvesting. Since the subsequent active fire detection thresholds rely directly on this σ, a 15-day window would significantly suppress sensitivity to low-temperature fires. Therefore, the 10-day period strikes the optimal balance between securing sufficient historical samples and maintaining background stability.

The accuracy of the mean and standard deviation in the historical background reference database can be compromised by the presence of cloud and fire contamination in the time-series data. To address these disturbances, this study sequentially applied cloud masking, fire pixel removal, and kσ filtering to exclude outliers [24,42,43]. The detailed procedure is described below: First, cloud pixels were identified and masked according to the algorithm (Formulas (1) and (2)) used by Zhang et al. [31], which exploits the combined spectral features of high reflectance in visible bands and low BT in TIR bands. These formulas utilize established empirical thresholds (e.g., 265 K, 285 K, 1.2, and 0.7) specifically optimized for the AHI to distinguish clear-sky land from cloud bodies. Next, fire-affected pixels were detected and removed based on the BT difference (BTD) between band 7 and band 14, following the method described by Lin et al. [44] with a BTD threshold of 20 K. Subsequently, an automated iterative kσ filter was applied to further exclude potential outliers, such as anomalously bright or dark pixels. In this process, any pixel with a BTD value beyond the range of $\mu \pm k\sigma$ (where k = 3) was considered an outlier and

removed [43]. This iterative process continued until no additional outliers were identified in the dataset. To demonstrate the effectiveness of this iterative approach, a representative case of outlier removal (at 34.28°S, 146.28°E) is illustrated in Figure 3. Notably, while the BTD of the outlier (index 6) was 13.9 K, well below the preliminary 20 K coarse threshold, it was successfully identified as a statistical outlier and removed during the first iteration (Figure 3c). By ensuring that only highly reliable observations are retained, the resulting dataset forms a statistically homogeneous population, where the arithmetic mean serves as a robust and unbiased estimator of the fire-free background state. Finally, the mean and standard deviation were calculated from the retained valid images to generate background reference database imagery for active fire detection.

$$(BT_{15} < 265K\ AND\ \rho_3 + \rho_4 > 1.2)\ OR\ (BT_{15} < 285K\ AND\ \rho_3 + \rho_4\ > 0.7) \quad (1)$$

$$BT_{15} < 265K\ AND\ BT_4 < 295K \quad (2)$$

where ρ_i and BT_i represent the reflectance and BT of the i band, respectively. Formula (1) was applied for daytime cloud detection, and Formula (2) was used for night.

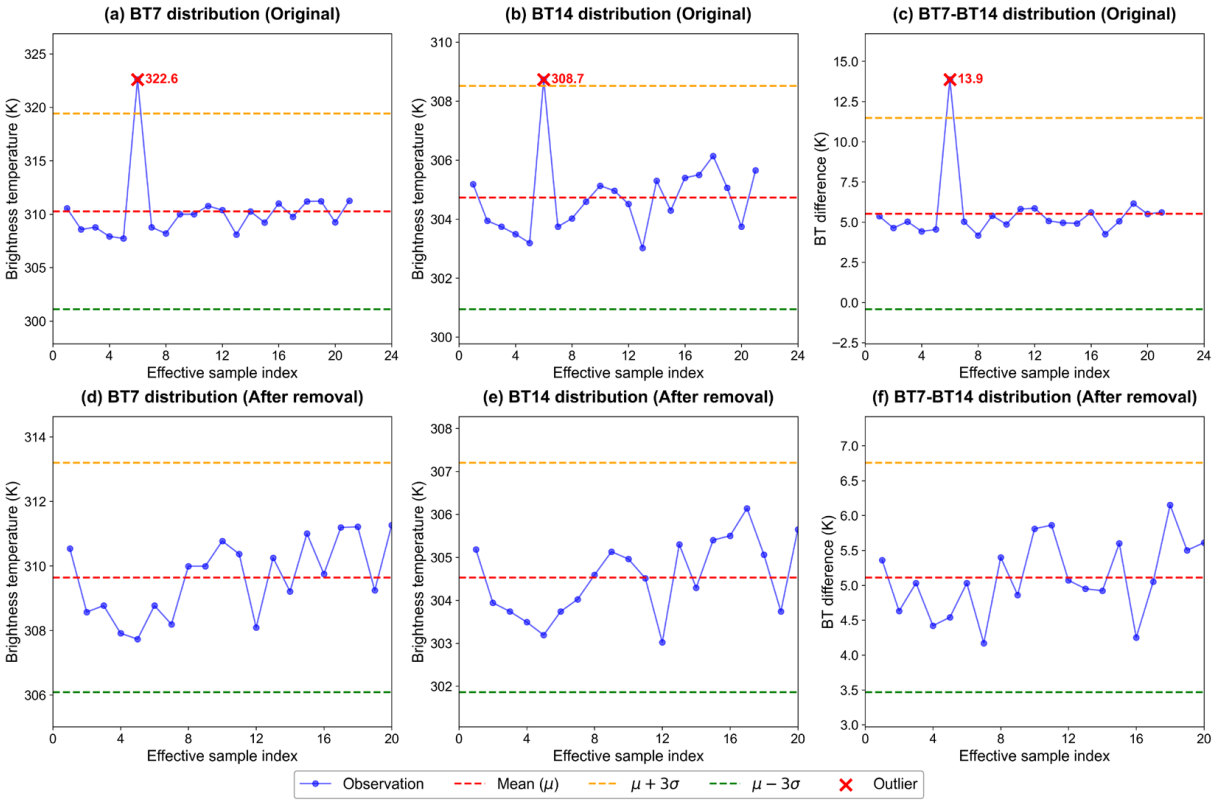


Figure 3. Illustration of the iterative kσ filtering process for a sample pixel (located at 34.28°S, 146.28°E): (**a**–**c**) show the original distributions of BT_7, BT_{14}, and the BT difference ($BT_7 - BT_{14}$), where a fire-contaminated outlier (index 6, BTD = 13.9 K) is identified by the 3σ criterion despite being below the 20 K coarse threshold; (**d**–**f**) show the distributions after removing the outlier, where the remaining 20 samples fall within the stable μ ± 3σ range, ensuring a clean and representative historical background baseline.

3.2. Active Fire Detection Algorithm Description

3.2.1. Cloud and Water Masking

Cloud masking is a critical step in almost all active fire detection algorithms. Overly sensitive cloud detection may misclassify dense fire smoke as clouds, leading to the erroneous removal of fire pixels; conversely, undetected clouds may be misidentified as

fire pixels due to specular reflection effects [10,21]. The fundamental principle of cloud masking schemes not only utilizes the spectral characteristics of clouds employed in Formulas (1) and (2) based on established thresholds [31,35], but also leverages the radiative contrast between cloud pixels and clear-sky land surfaces [25]. Therefore, this study enhanced the approach by incorporating the BTD of band 14 between the target image and the fire-free, clear-sky historical background reference database, enabling more effective identification and removal of residual cloud pixels. This historical baseline-based consistency check is defined as:

$$BT_{14} < 285K \; AND \; \frac{BT_{14} - \mu_{BT14_his_back}}{\delta_{BT14_his_back}} < -5 \tag{3}$$

where $\mu_{BT14_his_back}$ and $\delta_{BT14_his_back}$ represent the mean and standard deviation, respectively, of band 14 in the historical background reference database for the same time slot as the target image.

This check relies on the statistical purity of the historical background reference database. Since the historical mean ($\mu_{BT14_his_back}$) represents the expected clear-sky thermal state after purging outliers, a deviation of more than five standard deviations (<-5) provides a robust indicator of anomalous cloud cooling. Importantly, this $5\delta_{BT14_his_back}$ threshold provides a sufficient statistical tolerance to prevent the over-masking of fire smoke, which typically causes much smaller thermal deviations compared to actual cloud bodies. Quantitatively, evaluation of the smoke-obscured pixels demonstrates that smoke-induced cooling in band 14 is minimal, with deviations generally staying within -1σ of the historical mean. In contrast, cloud pixels exhibit significantly stronger negative deviations, consistently exceeding -5σ. The -5σ limit thus ensures a robust separation, preserving smoke-covered fire signals while effectively purging residual cloud contamination.

The water category from the International Geosphere-Biosphere Programme (IGBP) classification in the MODIS land cover type product (MCD12Q1) was utilized to initially separate water and land pixels. Furthermore, the following criterion was applied to identify residual water bodies (such as along coastlines) [31]:

$$NDVI < 0 \; AND \; \rho_6 < 0.05 \; AND \; \rho_4 < 0.15 \tag{4}$$

where NDVI denotes the Normalized Difference Vegetation Index, $NDVI = (\rho_4 - \rho_3)/(\rho_4 + \rho_3)$.

3.2.2. Active Fire Detection

According to the principles of active fire detection, pixels containing actively burning exhibit a sharp increase in radiance at 4 μm, while radiance at 11 μm also rises but to a lesser extent [45–47]. These spectral responses generate characteristic BT contrasts between the 4 μm and 11 μm bands relative to undisturbed background pixels, which serve as the primary indicators for spatial–contextual active fire detection method. Specifically, fire pixels are distinguished by higher BT values in both the 4 μm and 11 μm bands compared to valid background pixels, accompanied by a greater BTD between the two bands. Moreover, this observed BTD exceeds the corresponding BTD derived from valid background pixels [10,47]. Here, the term "valid background pixels" refers, in a spatially contextual (instantaneous) analysis, to adjacent land pixels that are confirmed to be free of clouds and fires; in a temporal (historical) analysis, it denotes pixels from the same geographic location in historical reference database.

1. Selection of valid background pixels

The identification of valid background pixels within a window centered on the target pixel is essential for reliable active fire detection, as these pixels provide the basis for

estimating the mean and standard deviation of background BT. An overestimated background values may lead to the omission of low-radiative fires, while an underestimated may increase false-alarm rates [10,18,47]. Quality control criteria were applied in this study to screen valid background pixels. First, eligible pixels must be cloud-free land surfaces and are not potential background fires. A pixel is classified as a potential background fire if the BTD between band 7 and band 14 exceeds 20 K [10,44]. Second, to mitigate contamination from the point-spread effect of adjacent fires, the eight immediate neighboring pixels surrounding the target pixel were excluded from the valid background set [24,25]. To ensure background statistics are derived from a representative sample size, if the proportion of valid background pixels within the analysis window (9 × 9 pixels) less than 20%, the target pixel was directly classified as non-fire.

2. Fire detection features

This study integrated instantaneous thermal-contrast features with historical background deviation features for robust active fire detection. The instantaneous features were derived from the differences between the target pixel's BT in the 4 μm band (BT_7), the 11 μm band (BT_{14}), and the inter-band BTD (ΔT) and the corresponding values of the valid background pixels, as defined in tests (5)–(8). The historical background features quantified the deviation of the observed ΔBT_7 (i.e., the difference between the target pixel's BT_7 and the mean BT_7 of valid background pixels) from its corresponding reference values in the historical background database, as expressed in tests (9) and (10). As defined in Section 3.1, if a pixel fails to meet the minimum sample size requirement ($N \geq 3$) due to persistent cloud cover, the algorithm degrades to rely exclusively on the instantaneous spatial–contextual features (Equations (5)–(8)). Under normal conditions with sufficient historical data, a pixel is identified as a fire pixel when all the following conditions are satisfied:

$$BT_7 > \overline{BT_7} + 3\delta_7 \tag{5}$$

$$\Delta T > \overline{\Delta T} + 3\delta_{\Delta T} \tag{6}$$

$$\Delta T > \overline{\Delta T} + 4K \tag{7}$$

$$BT_{14} > \overline{BT_{14}} - \delta_{14} \tag{8}$$

$$\Delta BT_7 > \Delta BT_{7_his_back} + 3\delta_{7_his_back} \tag{9}$$

$$\Delta BT_7 > \Delta BT_{7_his_back} + 5K \tag{10}$$

where $\overline{BT_7}$ and δ_7 are the mean and standard deviation of BT_7 for the valid background pixels; $\overline{BT_{14}}$ and δ_{14} are the mean and standard deviation of BT_{14} for the valid background pixels; $\overline{\Delta T}$ and $\delta_{\Delta T}$ are the mean and standard deviation of ΔT ($\Delta T = BT_7 - BT_{14}$) for the valid background pixels; ΔBT_7 denotes the instantaneous spatial contrast, defined as the difference between the target pixel's BT_7 and the surrounding background mean ($\overline{BT_7}$), i.e., $\Delta BT_7 = BT_7 - \overline{BT_7}$. Correspondingly, $\Delta BT_{7_his_back}$ represents the historical normal spatial contrast—the difference between the target pixel's historical mean $BT_{7_his_back}$ and its valid background mean ($\overline{BT_{7_his_back}}$), i.e., $\Delta BT_{7_his_back} = BT_{7_his_back} - \overline{BT_{7_his_back}}$; $\delta_{7_his_back}$ is the standard deviation of $BT_{7_his_back}$ for the valid background pixels in historical background reference database.

Equations (5)–(7) were employed to distinguish fire pixels from non-fire pixels. Test (8) was primarily designed to filter out small convective clouds, which exhibit lower BT in band 14 relative to the surrounding background. Additionally, this test aids in suppressing coastal false alarms that may arise when cooler water pixels are included in the valid background [46,48]. Notably, this study did not apply a BT threshold for band 7, as setting the threshold too high could lead to the omission of low-temperature fires [49].

Equations (9) and (10) define the core detection logic, which identifies fire pixels based on the historical deviation of the spatial–contextual difference. This approach overcomes the limitations of traditional dynamic change detection methods that rely on the temporal difference of absolute temperatures (e.g., $BT_7(t) - BT_7(t-1)$) [27,43]. While effective for detecting early-stage fires, such methods often fail during a fire's waning phase when temporal change is negligible [25], and are prone to misclassifying non-fire normal overheated conditions, such as particularly hot weather, as fire events [24].

Our dual-threshold design (3σ and 5 K) provides a robust solution to these challenges. The 3σ relative threshold accounts for pixel-specific historical variability ($\delta_{7_his_back}$), ensuring high sensitivity in stable, homogeneous landscapes (e.g., dense forests). The 5 K absolute threshold acts as a physical noise floor, preventing false alarms in extremely stable regions where the standard deviation is near zero. Physically, this spatial–contextual difference anomaly remains detectable regardless of the fire's temporal stage—whether intensifying or weakening—because the combustion-induced spatial contrast (ΔBT_7) consistently and abnormally disrupts the inherent spatial thermal structure represented by $\Delta BT_{7_his_back}$.

It is also worth noting the theoretical distinction between this proposed framework and pioneering historical baseline algorithms like the Robust Satellite Techniques for FIRES detection and monitoring (RST-FIRES) [24]. While RST-FIRES effectively utilizes historical baselines to detect fires (e.g., the space differential ALICE index), it relies predominantly on historical data and purely statistical thresholds (e.g., 5σ). Our approach advances this concept through two critical mechanisms. First, the strict dual-feature fusion—requiring simultaneous satisfaction of instantaneous constraints (Equations (5)–(8)) and historical deviations (Equations (9) and (10))—is crucial for suppressing unmasked residual clouds (e.g., warm clouds with high MIR solar reflectance). While such clouds often generate spurious fire signatures and trigger false alarms in purely historical anomaly indices, they are effectively screened out by our instantaneous contextual checks. Second, rather than relying on purely statistical thresholding, which is vulnerable to minor sensor noise in highly homogeneous regions where historical variance is near zero, our method couples the adaptive statistical threshold (3σ) with the strict physical noise floor (5 K), ensuring that the detected anomaly is both statistically and physically significant.

In the case of extremely hot weather, although both the target pixel and valid background pixels exhibit high BT, their difference does not increase substantially, thus preventing misclassification. Similarly, persistent non-fire anomalies, such as land-water edges or industrial heat sources, exhibit spatial contrasts that are consistent with their historical background ($\Delta BT_{7_his_back}$), resulting in a small deviation that does not trigger an alarm. Consequently, this spatiotemporal context index retains the high sensitivity of spatial–contextual algorithms while effectively suppressing false alarms associated with both instantaneous heterogeneity and absolute temperature fluctuations.

3.2.3. False Alarm Filter

To further enhance detection reliability, a post-processing step was implemented to eliminate residual false alarms arising from non-fire thermal anomalies, such as small warm clouds, cloud edges, and water boundaries. Fire pixels identified by the core algorithm were subjected to a series of validity tests. A pixel was reclassified as a false alarm if it satisfied any of the following criteria:

$$BT_7 < 300K \; AND \; BT_{14} < 280K \; AND \; BT_{14} - \overline{BT_{14}} < 0.5K - \delta_{14} \tag{11}$$

$$BT_7 < 310K \; AND \; \rho_3 > 0.2 \; AND \; \rho_4 > 0.3 \; AND \; \rho_3 > \; \rho_6 \tag{12}$$

Test (11) was designed to further remove cold clouds that exhibit lower BT in both the MIR and TIR bands, particularly when the TIR BT falls below the surrounding background. Condition (12) incorporates specific reflectance thresholds to exclude common false alarms, including thin and warm clouds. Although these features may display a modestly elevated MIR BT—comparable to that of a low-intensity fire—they are distinguished by higher reflectance in the visible and near-infrared bands. Furthermore, a strict spatial–contextual criterion was applied to eliminate cloud-edge and water-edge effects. Specifically, if any pixel within the 3×3 pixels window centered on a fire was classified as cloud or water, the central fire pixel was rejected as a probable boundary artifact. This conservative filtering approach ensures that only pixels with high confidence of being true active fires are retained in the final results.

3.3. Evaluation Method and Metrics

The algorithms performance evaluation was based on comparison with validated VIIRS active fire products from Suomi NPP and NOAA-20 satellites. The intercomparison procedure followed the spatiotemporal matching approach widely used in previous studies that employ polar-orbiting satellite data (e.g., VIIRS, MODIS) to assess the accuracy of geostationary satellite active fire monitoring (e.g., GOES, Himawari-8). Temporally, only VIIRS overpasses within ± 6 min of the Himawari-8/9 observation time were selected for matching. Spatially, owing to the higher spatial resolution of VIIRS, multiple VIIRS fire detections could fall within a single Himawari-8 pixel; therefore, VIIRS fire locations were reprojected onto the Himawari-8 grid. If multiple VIIRS fire pixels corresponded to the same Himawari-8 pixel during the matched time window, only one was retained as a valid reference to avoid spatial redundancy in the statistics. The matched VIIRS data were quantitatively compared to the Himawari-8/9 active fire detections. An omission error (OE) was counted when a VIIRS fire pixel had no corresponding Himawari-8/9 fire detection within a 3×3 window centered on the reprojected location. Conversely, if Himawari-8/9 detected a fire pixel, but no VIIRS fire pixel was found within the surrounding 3×3 window, it was recorded as a commission error (CE). A 3×3 pixel window (centered on the reprojected VIIRS fire location) was adopted for spatial matching, which is a standard and necessary protocol in cross-sensor validation. Due to the "bow-tie effect" at the edges of the VIIRS swath, geostationary parallax, and reprojection shifts, positional deviations between fire detections from different sensors are likely to occur. Consequently, strict 1×1 pixel matching is prone to severe mismatch errors. However, because this spatial displacement is generally expected to remain within the footprint of adjacent pixels, a 3×3 window—covering the target pixel and its eight immediate neighbors—provides an optimal buffer to accommodate all geometrically plausible matches. Using a larger window (e.g., 5×5) is unnecessary and risks inappropriately associating independent fire events.

It is important to note that while the validation year (2023) is encompassed within the multi-year period (2021–2024) used for historical database construction, this does not compromise validation independence. Because fire-affected pixels and thermal outliers were rigorously purged during the database construction phase (via the iterative kσ filtering), no target fire information leaked into the historical baseline. Including the fire-free data of the validation year simply ensures that the historical baseline accurately represents the contemporary land-cover and phenological state.

Based on the matching results, three evaluation metrics (including *OE*, *CE* and *F1-score*) were calculated as follows:

$$OE = \frac{FN}{TP + FN} \tag{13}$$

$$CE = \frac{FP}{TP + FP} \tag{14}$$

$$F1\text{-}score = 2 \times \frac{precision \times recall}{precision + recall} \tag{15}$$

where TP (true positives) is the number of correctly classified fire pixels; FN (false negatives) is the number of fires incorrectly classified as non-fire pixels; and FP (false positives) is the number of non-fires incorrectly classified as fire pixels; $precision = 1 - CE$ and $recall = 1 - OE$.

4. Results

4.1. Qualitative Analysis in Representative Scenarios

The performance of the proposed algorithm was evaluated across diverse fire events that vary in intensity and type, with comparative analyses conducted relative to the operational Himawari-8/9 WLF product. These specific cases were deliberately selected as they represent extreme edge cases (e.g., low-temperature or smoke-obscured environments) that are notoriously challenging for traditional algorithms, thereby serving to effectively illustrate the boundaries of algorithmic sensitivity.

1. Low-temperature fire cases

Low-intensity fires and small-scale fires often exhibit low-temperature characteristics, with BT potentially falling below the detection threshold for band 7, making them prone to being missed by conventional methods. Figure 4 presents the detection results for two fire events on 12 April 2023 (UTC 07:10) and 14 April 2023 (UTC 04:50), both located in high-latitude regions near the edge of Himawari-8/9 imagery. For instance, taking the case in Figure 4(a1), while the target pixel's absolute BT_7 was only 294.72 K, the surrounding background mean was 287.77 K. This yields a pronounced spatial contrast (ΔBT_7) of 6.95 K, functioning as a strong thermal signal-to-noise ratio. This pronounced BTD persists between the fire pixels and their surrounding background, which provides a robust indicator for fire identification. The spatial–contextual difference features adopted in this study effectively detected these low-temperature fires, while the Himawari-8/9 WLF product failed to capture them. These detections are further supported by corresponding VIIRS active fire product and contemporaneous Sentinel-2 imagery, which visually confirm active burning in the same locations.

2. Fire detection under dense smoke

Previous studies have shown that the omission of fire pixels obscured by dense smoke is a frequent challenge in satellite-based fire detection algorithms, primarily attributable to imperfect cloud screening [21,36]. This interference hinders the early detection of small-scale fires and constrains the spatiotemporal accuracy of fire-progression mapping [50]. Figure 5 illustrates representative cases of fires under thick smoke and thin cloud on 12 July 2023 (UTC 03:40). Under these challenging conditions, the proposed algorithm demonstrates superior robustness than the operational WLF product, detecting a greater number of confirmed fire pixels. Specifically, in the sub-cloud fire case shown in Figure 5(a1), although thin cloud attenuated the absolute BT of the fire pixel, the spatial contrast (ΔBT_7) remained robust at 8.41 K, successfully exceeding the historical deviation threshold (6.83 K). Consequently, both the VIIRS active fire product and our algorithm successfully identified the fires, while the WLF product likely missed them owing to excessive cloud-masking. The fire pixels in Figure 5(a2,a3), though not flagged by the VIIRS product, were visually confirmed as actively burning in contemporaneous Sentinel-2 imagery. Furthermore, Figure 5(b1,b2) exemplify CE generated by the WLF product along burn-scar

edges and over built-up areas, respectively—errors that were effectively avoided by the proposed algorithm.

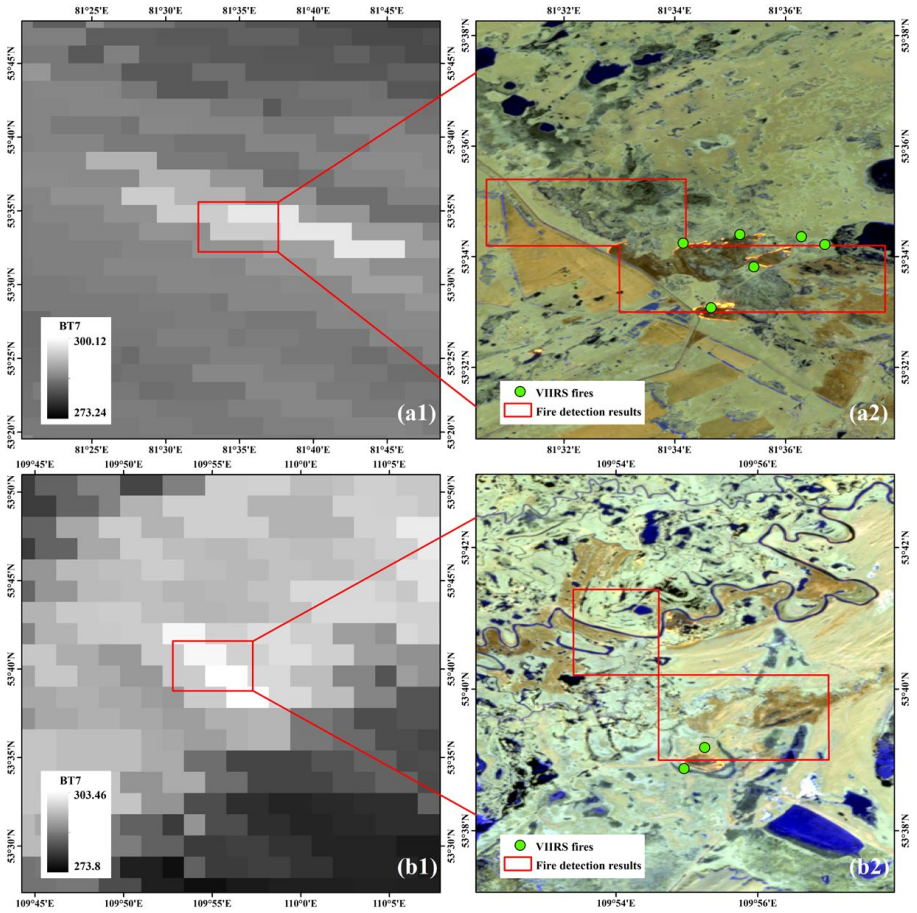


Figure 4. Low-temperature fire detection results on 12 April 2023 (UTC 07:10) and 14 April 2023 (UTC 04:50). (**a1**,**b1**) show the BT in band 7 for the two cases; (**a2**,**b2**) present the detection results from the proposed algorithm and the VIIRS fire product, overlaid on Sentinel-2 false-color composite (bands 12, 11, and 8A) imagery.

3. Early fire detection case

Timely and accurate detection of early-stage fires is critical for enabling effective fire suppression and mitigating potential damage. Due to their typically small scale and low intensity, early fire pixels often produce weak radiative signals within the relatively coarse spatial resolution of Himawari-8/9 imagery, making them susceptible to omission. Figure 6 shows a fire event in Australia on 18 April 2023, which exhibited a dynamic cycle of "ignition–extinction–re-ignition." The fire initially appeared at UTC 05:00, extinguished by UTC 05:50, and re-ignited at UTC 06:10. The proposed algorithm successfully captured the initial fire signal at UTC 05:00, where the absolute BT_7 was approximately 312.91 K and the spatial contrast ΔBT_7 reached 6.23 K, significantly exceeding the historical norm 0.12 K. Our algorithm continuously tracked it through subsequent burning phases, except at 05:20 UTC and 06:00 UTC when the signal was extremely weak. The Suomi NPP VIIRS satellite also identified the fire during its overpass at UTC 05:46. In contrast, the WLF product did not report the fire until UTC 06:10, representing a detection delay of approximately 70 min compared to our algorithm. This case highlights the capability of the proposed method to continuously monitor early-stage, intermittent small fires at high temporal resolution, supporting real-time warning and dynamic tracking.

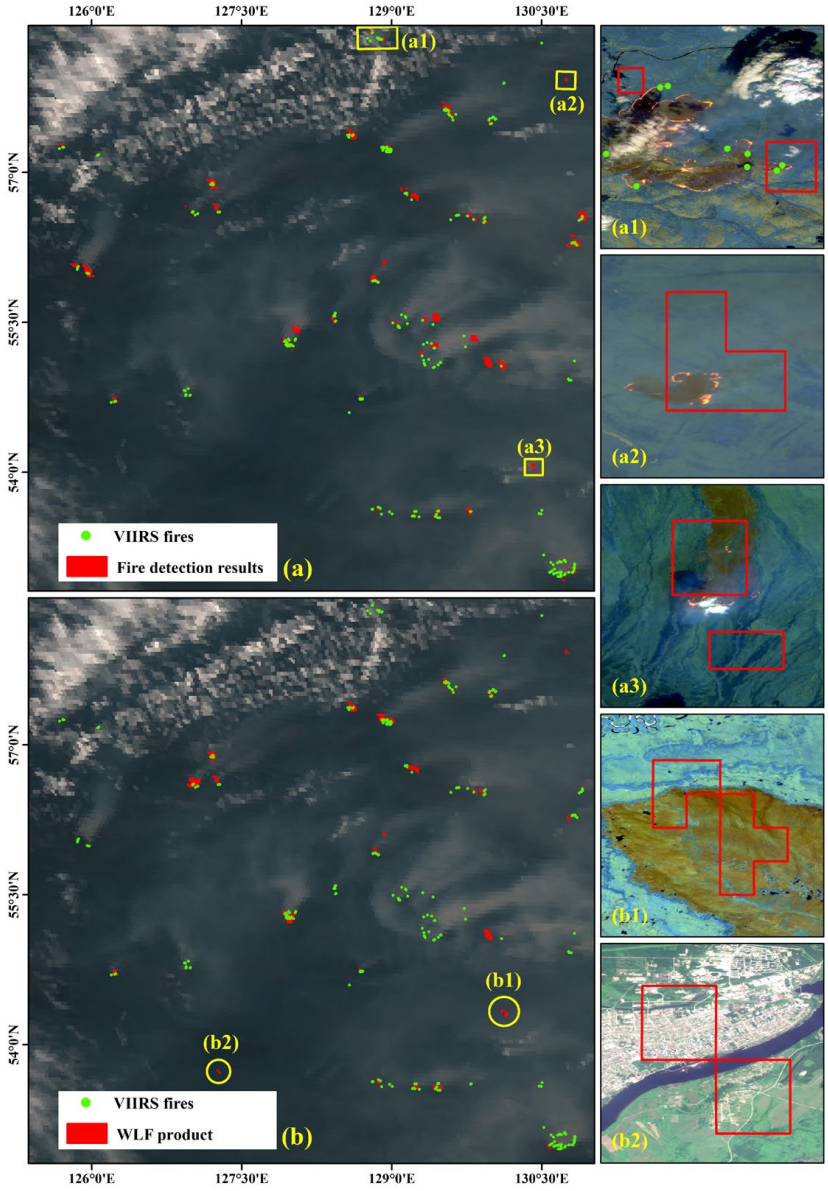


Figure 5. Fire detection performance under dense smoke on 12 July 2023 (UTC 03:40). (**a**) shows the detection results from the proposed algorithm compared with the VIIRS active fire product; (**b**) presents detections from the WLF product alongside the same VIIRS reference data; (**a1**–**a3**) illustrate zoomed-in views of actual fires (red boxes) correctly identified by the proposed algorithm in selected sub-regions (yellow rectangles in (**a**)); (**b1**,**b2**) show zoomed-in views of false alarms (red boxes) generated by the WLF product in selected sub-regions (yellow circles in (**b**)).

4.2. Overall Quantitative Validation

Table 1 presents the overall performance validated against more than 55,000 verified VIIRS fire detections. The results demonstrated that the proposed algorithm achieves significant improvements over the Himawari-8/9 WLF product in terms of false-alarm suppression, detection accuracy, and overall reliability. Specifically, the CE is dramatically reduced from 23.3% (WLF) to 2.9%, representing a relative decrease of 87.6%. Meanwhile, the OE is lowered from 57.0% to 37.5%, corresponding to a 34.2% relative improvement. Importantly, while effectively suppressing false alarms, the proposed algorithm maintains high detection accuracy of actual fires, raising the F1-score from 0.55 to 0.76—a relative gain of 38.2%. It should be noted that owing to the massive validation sample size (N = 55,561), the 95% confidence intervals for all reported point estimates (e.g., CE and OE), calculated based on a binomial distribution, are extremely narrow (with a margin of error < $\pm$0.5%).

This confirms that the observed performance improvements over the operational WLF product are highly statistically significant.

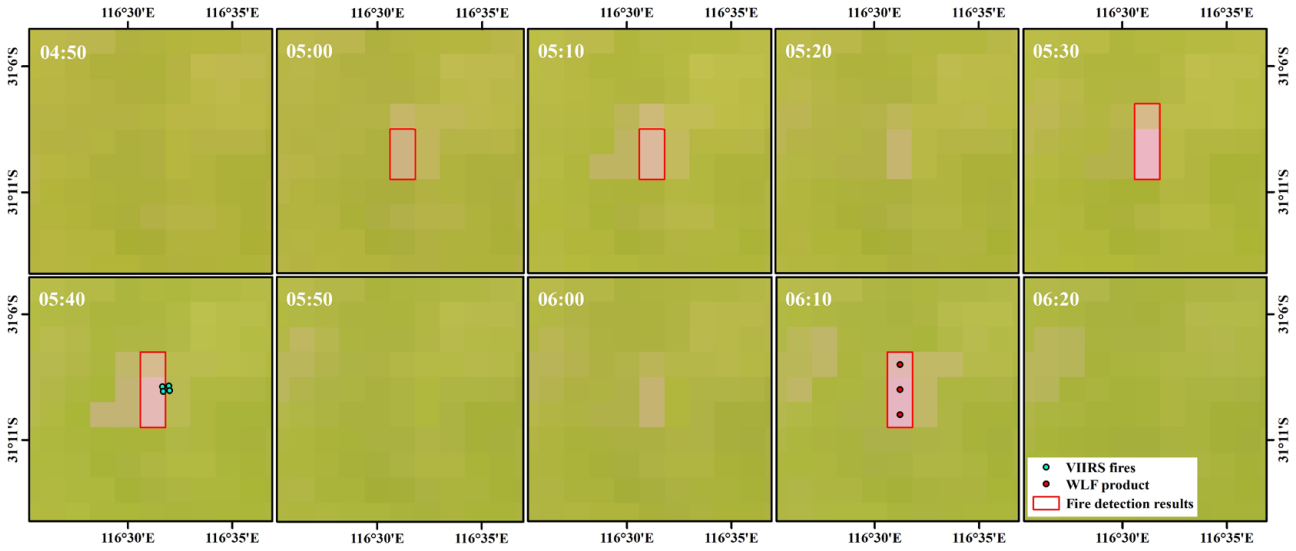


Figure 6. Early fire detection results. Comparison between detections from the proposed algorithm and the WLF product across multiple phases of an intermittent agricultural fire event in Australia on 18 April 2023. The base image is a false-color composite where RGB corresponds to band 7 BT, band 14 BT, and their BTD.

Table 1. Performance comparison between the proposed method and the WLF product.

Metric	WLF Product	Proposed Method	Relative Improvement
OE	57.0%	37.5%	−34.2%
CE	23.3%	2.9%	−87.6%
F1-score	0.55	0.76	+38.2%

Figure 7 illustrates typical false alarms generated by the WLF product over urban persistent heat sources. Figure 7a summarizes the spatial distribution of false detections during the period UTC 05:30–05:50 on 16 April 2023, which corresponds to local afternoon with strong surface heating. Compared with surrounding farmland, artificial surfaces (e.g., buildings, roads) possess lower thermal inertia and thus warm up more rapidly, resulting in higher BT than adjacent agricultural pixels, as shown in the BT_7 image at UTC 05:40 in Figure 7b. Such distinct spatial–contextual BT contrast, caused by differences in surface thermal properties, are prone to be misclassified as fires by algorithms that rely solely on single-time-slot imagery. By incorporating spatial–contextual difference features derived from the historical background reference database, the proposed method effectively suppresses such false alarms. Because the thermal radiation characteristics of urban areas remain relatively stable over time, similar spatial–contextual BT contrast patterns also appear in historical background imagery from the same period (e.g., the second ten-day period of April at UTC 05:40, shown in Figure 7c). Comparing the spatial–contextual differences between the target image and the historical reference data reveals only minor discrepancies for these pixels, which are therefore correctly classified as non-fire. In contrast, true fire pixels exhibit pronounced temporal variations in spatial–contextual differences, enabling reliable detection.

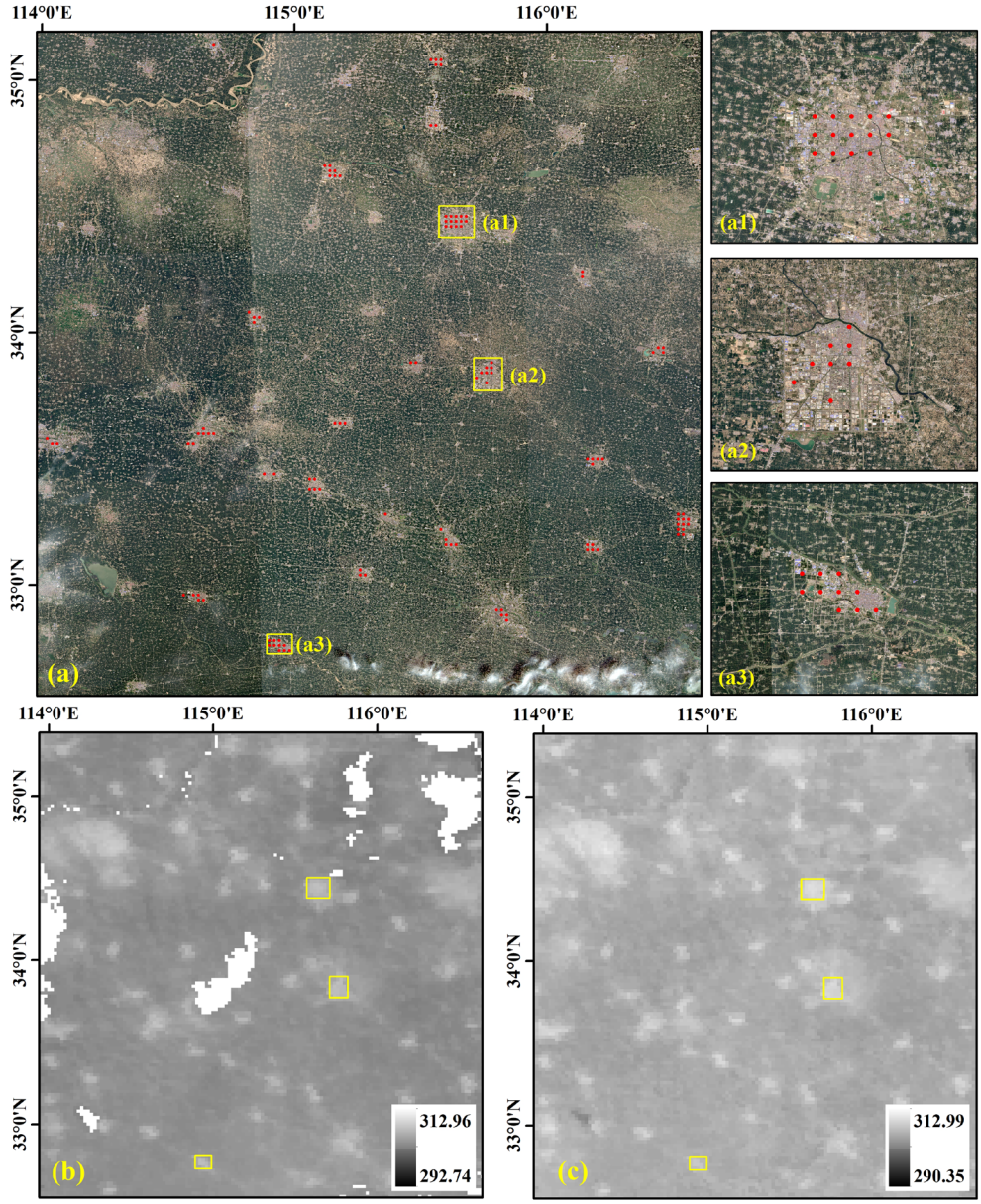


Figure 7. Illustration of false alarms in the WLF product. (**a**) shows spatial distribution of false detections during UTC 05:30–05:50 on 16 April 2023, (**a1**–**a3**) are zoomed-in views of selected sub-regions; (**b**) displays the band 7 BT at UTC 05:40; (**c**) presents the corresponding historical background reference BT for band 7 (same period as (**b**)). The yellow boxes in (**b**,**c**) indicate the same sub-regions shown in (**a1**–**a3**).

The validation in this study was based on the VIIRS active fire product, which has a higher spatial resolution (375 m) with a pixel area approximately 1/28 of that of Himawari-8/9. As a result, the same fire occupies a much smaller area fraction within a Himawari-8/9 pixel, leading to a reduced fire-to-background radiative energy ratio. Some low-intensity fires may even produce no detectable thermal signal in Himawari-8/9 observations. When validated against VIIRS fire pixels as reference truth, the proposed algorithm achieved a recall of 62.5%. Although this detection performance is inherently limited by the spatial resolution mismatch, it remains significantly higher than that of the WLF product (43%), demonstrating the algorithm's ability to detect a larger number of actual fire events.

To further contextualize the OE and disentangle algorithmic limitations from the inherent physical detection limits of the 2 km AHI sensor, we conducted a sub-pixel stratified assessment. Table 2 illustrates the OE as a function of the sub-pixel fire scale,

quantified by the number of 375 m VIIRS fire pixels co-located within a single Himawari-8/9 pixel. The stratified results reveal a pronounced sub-pixel effect. Approximately 50% of the validation dataset consists of micro-fires represented by a single VIIRS pixel. At this scale, the fire radiative signal is heavily diluted by the surrounding non-fire background, leading to inherently high OEs for both our algorithm (61.2%) and the WLF product (74.2%). This indicates that the overall OE is heavily weighted by physically undetectable micro-fires. However, as the sub-pixel fire scale increases, the proposed algorithm demonstrates overwhelming superiority. As the number of embedded VIIRS pixels increases from 2 to 10, the OE of the proposed algorithm drops dramatically and monotonically to below 10%, highlighting its exceptional sensitivity to emergent and growing fires. In stark contrast, the WLF product fails to exhibit a proportional improvement, maintaining a high OE of over 50% even when encompassing up to 14 VIIRS pixels. This stratified analysis validates that the proposed dual-feature framework not only effectively suppresses false alarms but also maximizes the true detection capabilities within the physical constraints of geostationary spatial resolution.

Table 2. Stratified assessment of OE based on the number of VIIRS fire pixels within a Himawari-8/9 pixel.

Number of VIIRS Fire Pixels Per Himawari-8/9 Pixel	Proportion of Verified Fires (%)	OE of Proposed Algorithm (%)	OE of WLF Product (%)
1	50.0	61.2	74.2
2	22.6	48.6	66.3
3	10.7	37.8	59.2
4	6.1	31.4	56.6
5	3.8	28.4	56.0
6	2.3	20.6	51.8
7	1.4	14.9	52.8
8	0.9	16.5	52.5
9	0.7	11.6	55.6
10	0.4	9.5	56.5
11–14	0.8	8.1	60.1
≥15	0.3	0	68.2

4.3. Performance Analysis Across Fire Types and Algorithmic Boundaries

4.3.1. Performance Comparison Across Different Fire Categories

We further evaluated the algorithm's performance across different fire types, as summarized in Table 3. The results showed that the proposed algorithm consistently outperforms the WLF product across all fire categories. Specifically, the algorithm achieved detection rates above 62% for forest, shrubland, and grassland fires. Notably, our algorithm shows a significant advantage in forest fire detection (62.1% vs. 38.5% for WLF). This is primarily because forest fires are often accompanied by dense smoke; while the WLF product often misses these events due to overly sensitive cloud masking, our spatial–contextual design retains higher robustness under smoke-obscured conditions.

Table 3. Comparison of fire detection performance between the proposed method and the WLF product across different fire types.

Fire Type	Total Number	Proposed Method Detections (Detection Rate)	WLF Product Detections (Detection Rate)
Forest fire	10,065	6247 (62.1%)	3878 (38.5%)
Shrubland fire	9799	6266 (63.9%)	4238 (43.2%)
Grassland fire	28,643	19,040 (66.5%)	12,891 (45.0%)
Cropland fire	6835	3095 (45.3%)	2794 (40.9%)
other	219	85 (38.8%)	101 (46.1%)

However, both algorithms exhibit a relative performance drop for cropland fires (45.3% for the proposed method), indicating a common challenge in monitoring agricultural burning at the 2 km geostationary resolution. To better understand the drivers behind these performance discrepancies, it is essential to provide a detailed examination of the physical and algorithmic boundaries that constrain detection capabilities.

4.3.2. Failure Case Analysis

To provide a comprehensive evaluation and fully characterize the algorithm's operational limitations, this section analyzes a representative failure case in Southeast Asia and eastern India, regions which exhibit the highest concentration of agricultural fire activity within the Himawari-8/9 coverage area. Driven by climate conditions and crop cultivation cycles, April marks the peak season for agricultural fires in these regions. Figure 8 illustrates the monitoring results for this area, comparing (a) the proposed algorithm and (b) the WLF product against the VIIRS fire product. It is evident that a substantial portion of fires recorded by the 375 m VIIRS sensor remain undetected by both the proposed algorithm and the WLF product.

This systemic failure highlights the absolute physical boundaries of the 2 km Himawari-8/9 AHI sensor, driven by three primary factors: (1) Sub-pixel scale limitation: Agricultural fires are typically small-scale. Based on our stratified assessment (Table 2), the majority of these undetected cropland fires occupy only a single VIIRS fire pixel. Within the 4 km^2 footprint of an AHI pixel, the radiative energy from such micro-fires is heavily diluted by the non-fire background, making them physically undetectable regardless of the algorithmic logic. (2) Edge-of-disk geometric effects: This region is located at the edge of the Himawari-8/9 observation disk, corresponding to large viewing zenith angles. This geometry leads to coarser effective spatial resolution and longer atmospheric transmission paths, which further attenuate the weak thermal signatures of crop fires. (3) Temporal sampling mismatch: Agricultural fires often exhibit transient combustion characteristics with short durations. There is a physical mismatch between these brief events and the 10-min sampling frequency of Himawari-8/9. If the peak combustion phase occurs between scans, or if the fire intensity wanes rapidly before the next observation slot, the algorithm may fail to capture a thermal signal that is statistically distinct from the background. This temporal mismatch is further highlighted when validating against instantaneous polar-orbiting snapshots like VIIRS, leading to omission errors for short-lived fire events. Identifying these failure scenarios is crucial, as it suggests that while geostationary sensors provide unmatched temporal frequency, they must be supplemented by higher-resolution polar-orbiting data to achieve comprehensive monitoring of small-scale agricultural activities.

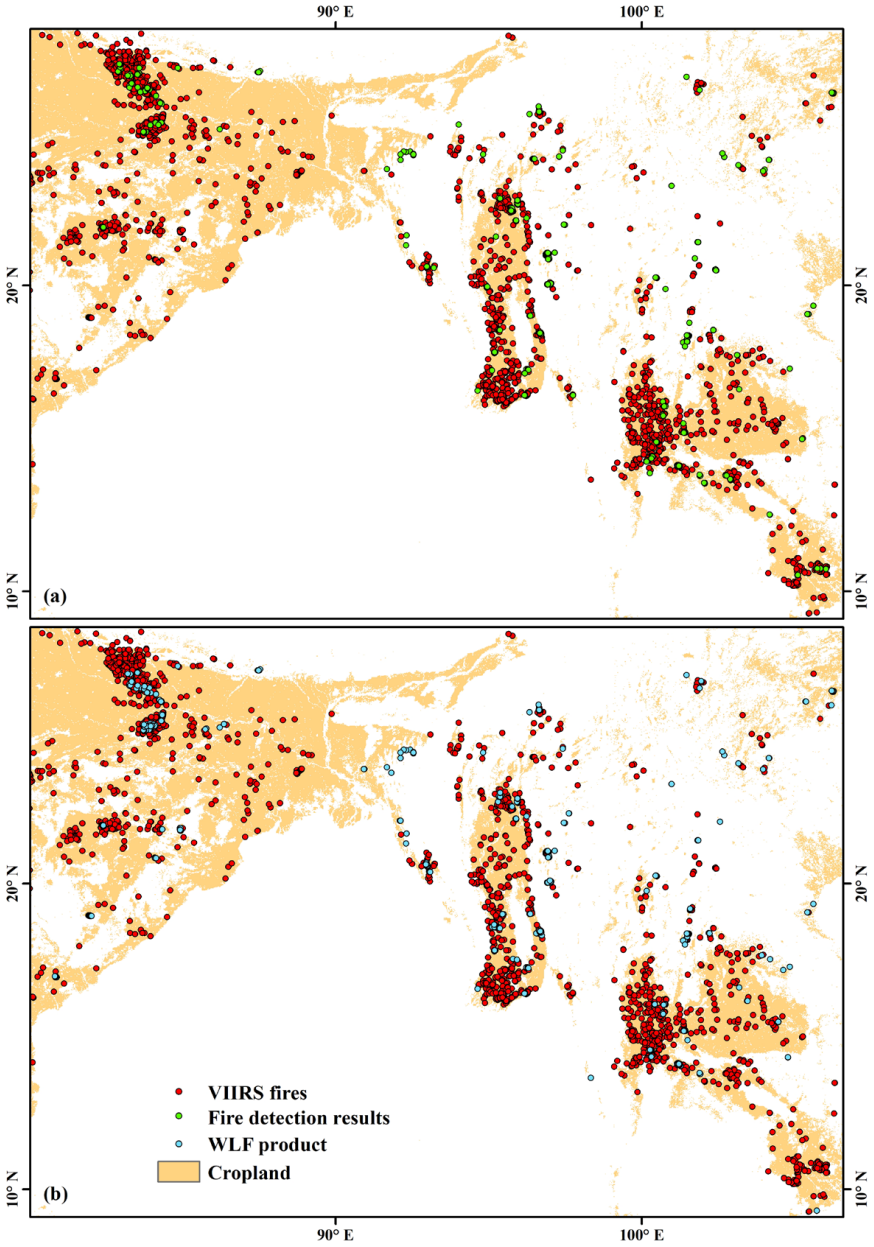


Figure 8. Comparison of agricultural fire detection results in Southeast Asia and eastern India: (**a**) Results from the proposed algorithm versus the VIIRS active fire product; (**b**) WLF product versus the VIIRS active fire product.

5. Discussion

5.1. Robustness of the Historical Background Reference

As a fire-free baseline, the quality of the historical background reference database significantly influences the accuracy of active fire detection. To evaluate its performance, this study assesses the database's reliability from two perspectives: time-series analysis and a comparative assessment against actual observed data.

To verify the temporal consistency of the mean BT values within the background reference database, sample points representing typical land cover types—forest, shrubland, grassland, and cropland—were selected. The mean BT values at various diurnal observation times were extracted to analyze whether their temporal variations align with surface thermodynamic principles. Figure 9 illustrates the diurnal variation curves of the background mean BT and the BTD (BT7 − BT14) during mid-July. As shown, both the

BTs of band 7 and band 14, as well as their difference, are significantly higher during the daytime than at night. Specifically, band 7 exhibits higher BTs than band 14 during the day, whereas the difference between the two bands diminishes at night. This phenomenon is mainly driven by solar radiation. During the day, solar heating causes a significant rise in BT for both bands; however, band 7 is more sensitive to solar radiation, resulting in more intense variations. Consequently, the temperature difference between the two bands increases due to this differential heating effect. Following sunset, the BTs of both bands gradually decrease and stabilize, remaining essentially constant throughout the night.

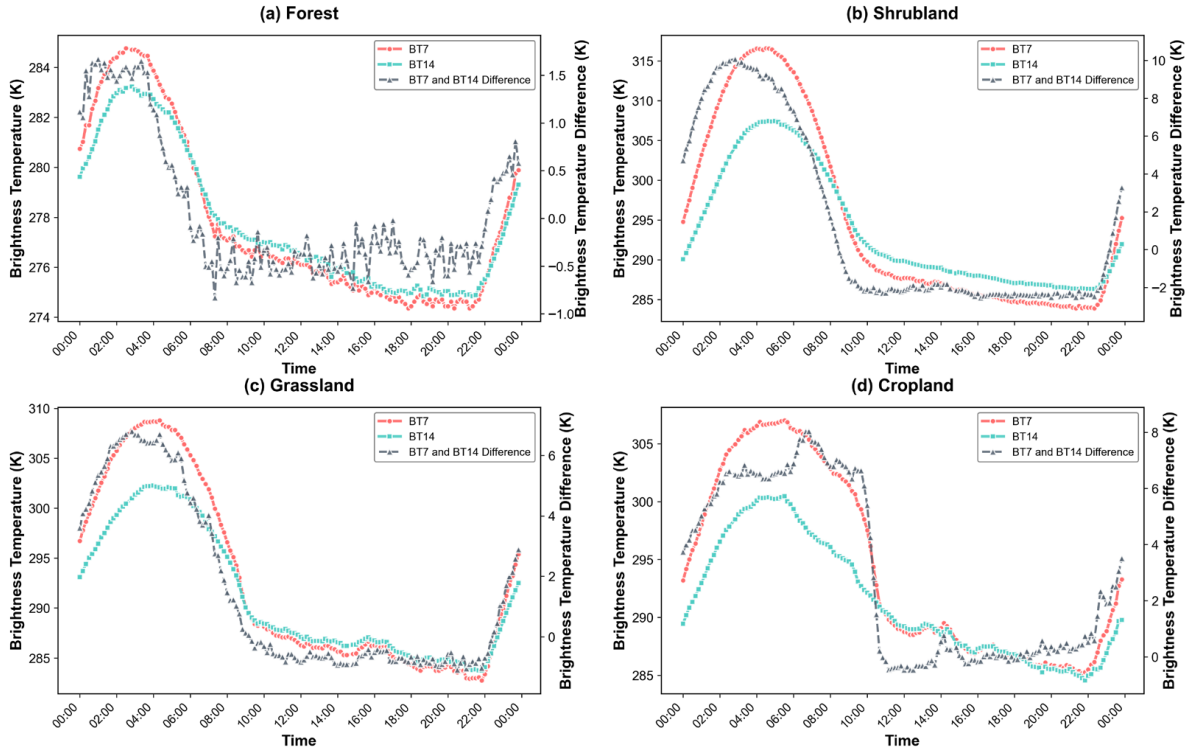


Figure 9. Diurnal variations of mean BTs (band 7 and band 14) and their difference across representative land cover types: (**a**) Forest, (**b**) Shrubland, (**c**) Grassland, and (**d**) Cropland.

Furthermore, it is evident that homogeneous surfaces, such as forests, exhibit lower BT differences, whereas highly heterogeneous surfaces, like shrublands, display larger differences. This is primarily attributed to the presence of bare soil within shrubland areas. Due to its rapid thermal response to solar radiation, the exposed soil heats up quickly, resulting in higher daytime temperatures and a consequently larger temperature contrast. In summary, the diurnal BT variations across different land cover types are consistent with thermodynamic laws, supporting the rationality and reliability of the background reference database.

To further evaluate the quality of the historical background reference database, we compared the historical mean BT with corresponding actual measurements. Multiple samples were randomly selected within the Himawari-8/9 coverage area, from which observed BT values and their corresponding statistical characteristics from the background reference database were extracted across various seasons and locations. The comparison results are presented in Figure 10. It can be observed that in the absence of fire events, the difference between the measured BT and the historical mean is minimal, indicating that the database accurately captures the actual thermal conditions of the surface. Conversely, for pixels containing fires, both the observed BT7 and the BT difference are significantly higher than the corresponding historical reference statistical values. These results further

demonstrate that the constructed historical background reference database provides a robust foundation for effective fire monitoring.

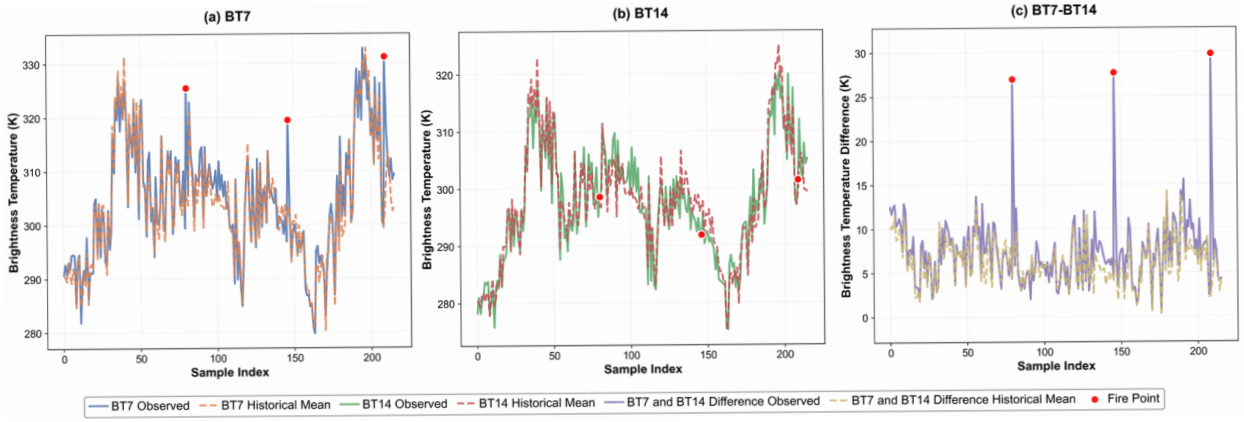


Figure 10. Comparison between statistical characteristics from the background reference database and corresponding actual measurements. (**a**–**c**) show the comparisons of observed vs. historical mean values for band 7 BT, band 14 BT, and their BTD, respectively.

5.2. Performance Drivers and Limitations

The significant reduction in both OE and CE (each lowered by approximately 20%) along with the increased F1-score collectively confirmed that the proposed algorithm substantially improves fire detection reliability relative to the operational WLF product. This performance gain is primarily driven by two synergistic mechanisms. First, the notably low CE highlights the effectiveness of suppressing inherent surface heterogeneity, which treats persistent, high-contrast landscape features (e.g., urban heat sources or vegetation-soil boundaries) as static background components. By benchmarking against the intrinsic thermal signature of each pixel, the algorithm effectively differentiates transient fire signals from persistent non-fire anomalies that typically confound monophase spatial methods. Second, the marked decrease in OE is attributed to the enhanced sensitivity of the multi-stage framework. Specifically, the implementation of a smoke-tolerant cloud masking protocol prevents smoke-covered fires from being prematurely excluded. Furthermore, by adopting this spatial–contextual differences anomaly detection approach rather than relying on rigid absolute BT limits, the algorithm successfully identifies low-temperature or early-stage fires that exhibit weak absolute intensities but remain statistically distinct from both their immediate surroundings and long-term historical norms.

Despite these improvements, the performance of the proposed algorithm is subject to several constraints. First, the construction of the historical background reference database requires a sufficiently long time-series of cloud-free observations, which may be a limiting factor during the early operational phase of a satellite mission when statistically robust reference fields cannot yet be derived from limited clear-sky data. Second, the representative accuracy of the historical baseline may be compromised by the Earth's spatiotemporal dynamics. On one hand, rapid land-cover changes (e.g., urbanization or deforestation) can permanently alter the local thermal characteristics. On the other hand, extreme interannual climate variability (e.g., severe droughts or heatwaves) may cause highly heterogeneous surfaces to heat asymmetrically due to differing thermal inertias. Both factors can stretch spatial temperature contrasts beyond established thresholds, potentially triggering false alarms. To mitigate this, future work will investigate the integration of dynamic NDVI pre-filters and real-time meteorological correction factors (e.g., soil moisture anomalies). Third, the algorithm faces physical, geometric, and temporal boundaries. As analyzed in Section 4.3.2, ultra-small sub-pixel fires remain difficult to resolve, especially at large viewing zenith angles near the disk edge where signal dilution is maximized. Furthermore,

the transient nature of certain fire types (e.g., short-lived agricultural residue burning) poses a temporal sampling challenge; if the peak combustion phase is shorter than or misaligned with the 10-min observation cycle, the fire may be missed even with high-frequency monitoring. Finally, the reliance on a fixed 9×9 spatial window—specifically the requirement for at least 20% valid background pixels—poses a challenge during large-scale fire events where the fire may saturate the entire local context. Future work will explore the use of multi-scale adaptive windows and the integration of multi-source satellite data to ensure detection robustness across all fire scales and durations.

Regarding operational deployment, several technical factors merit further consideration. First, in terms of computational complexity, the proposed algorithm is highly optimized for NRT applications. Because the multi-year historical database is pre-calculated offline, the online detection phase relies on pixel-wise band math and thresholding. This architecture is highly parallelizable; in operational testing, full-disk processing is completed in less than one minute, providing robust support for the 10-min high-frequency observation cycle of Himawari-8/9. Second, regarding sensor transferability, while the dual-feature theoretical framework is universal, migrating this algorithm to other geostationary sensors (e.g., GOES-R ABI or FY-4 AGRI) requires constructing sensor-specific historical databases that account for different spectral response functions (SRFs). Finally, regarding diurnal performance variations, it should be noted that while our overall validation ($N > 55{,}000$) encompasses both day and night data, the algorithm inherently performs with even higher reliability at night due to cooler backgrounds and the absence of solar interference. We focused our case studies on daytime scenarios as they represent the most challenging environments for false-alarm suppression.

6. Conclusions

To address the high false alarm rate in active fire detection caused by the inability of traditional methods to decouple fire-induced anomalies from inherent surface thermal heterogeneity, this study established a ten-day historical background reference database and developed a dual-feature fusion algorithm for Himawari-8/9. The framework integrates instantaneous spatial–contextual differences with historical deviations of these differences, utilizing the database as a stable, fire-undisturbed benchmark for anomaly detection. The algorithm was validated against a robust dataset of over 55,000 fire pixels, rigorously cross-verified using 10 m Sentinel-2 burn-scar data across diverse seasons and geographic regions.

The results demonstrated that the proposed algorithm significantly outperforms the operational WLF product. Specifically, it achieved a CE of 2.9% (an 87.6% relative reduction) and an OE of 37.5% (a 34.2% relative reduction), with a final F1-score of 0.76. A sub-pixel stratified assessment confirmed that the algorithm drastically improves detection probability as fire scale increases, while remaining constrained by the absolute physical limits of the 2 km sensor for ultra-small, single-VIIRS-pixel fires. Nevertheless, the algorithm exhibits exceptional robustness in challenging scenarios, including low-temperature, smoke-obscured, and early-stage fires.

The dual-feature fusion approach proposed in this study not only achieves high detection accuracy but is also highly optimized for operational use; in testing, the algorithm completed full-disk fire detection in less than one minute, fully supporting NRT requirements. This transferable framework provides a technical foundation for the development of a global coordinated fire monitoring system based on geostationary satellites. Future work will focus on implementing dynamic meteorological corrections, developing adaptive update mechanisms for the background reference database, and conducting

multi-year validations to further enhance the algorithm's reliability in a rapidly changing global climate.

Author Contributions: X.L. conceived and designed the study, wrote the first draft, analyzed the data, and collected all the study data; Y.M. provided critical insights into editing the manuscript. All authors have read and agreed to the published version of the manuscript.

Funding: This research was funded by the National Natural Science Foundation of China, grant number 42271412.

Data Availability Statement: The raw data supporting the conclusions of this article will be made available by the authors on request.

Acknowledgments: The authors would like to thank the Japanese Meteorological Agency, NASA, and the Copernicus Data Space Ecosystem for the availability of satellite data.

Conflicts of Interest: The authors declare no conflicts of interest.

References

1. Hong, Z.; Tang, Z.; Pan, H.; Zhang, Y.; Zheng, Z.; Zhou, R.; Ma, Z.; Zhang, Y.; Han, Y.; Wang, J.; et al. Active fire detection using a novel convolutional neural network based on Himawari-8 satellite images. *Front. Environ. Sci.* **2022**, *10*, 794028. [CrossRef]
2. Ramo, R.; Roteta, E.; Bistinas, I.; van Wees, D.; Bastarrika, A.; Chuvieco, E.; van der Werf, G.R. African burned area and fire carbon emissions are strongly impacted by small fires undetected by coarse resolution satellite data. *Proc. Natl. Acad. Sci. USA* **2021**, *118*, e2011160118. [CrossRef]
3. Liu, Y.; Zhi, W.; Xu, B.; Xu, W.; Wu, W. Detecting high-temperature anomalies from Sentinel-2 MSI images. *ISPRS J. Photogramm. Remote Sens.* **2021**, *177*, 174–193. [CrossRef]
4. Jones, M.W.; Abatzoglou, J.T.; Veraverbeke, S.; Andela, N.; Lasslop, G.; Forkel, M.; Smith, A.J.P.; Burton, C.; Betts, R.A.; van der Werf, G.R.; et al. Global and regional trends and drivers of fire under climate change. *Rev. Geophys.* **2022**, *60*, e2020RG000726. [CrossRef]
5. Xiang, M.; Xiao, C.; Feng, Z.; Ma, Q. Global distribution, trends and types of active fire occurrences. *Sci. Total Environ.* **2023**, *902*, 166456. [CrossRef]
6. Wooster, M.J.; Roberts, G.J.; Giglio, L.; Roy, D.P.; Freeborn, P.H.; Boschetti, L.; Justice, C.; Ichoku, C.; Schroeder, W.; Davies, D.; et al. Satellite remote sensing of active fires: History and current status, applications and future requirements. *Remote Sens. Environ.* **2021**, *267*, 112694. [CrossRef]
7. Haque, K.M.S.; Uddin, M.; Ampah, J.D.; Haque, M.K.; Hossen, M.S.; Rokonuzzaman, M.; Hossain, M.Y.; Hossain, M.S.; Rahman, M.Z. Wildfires in Australia: A bibliometric analysis and a glimpse on 'black summer' (2019/2020) disaster. *Environ. Sci. Pollut. Res.* **2023**, *30*, 73061–73086. [CrossRef]
8. Kang, Y.; Jang, E.; Im, J.; Kwon, C. A deep learning model using geostationary satellite data for forest fire detection with reduced detection latency. *GIScience Remote Sens.* **2022**, *59*, 2019–2035. [CrossRef]
9. Zhao, Y.; Ban, Y.; Sullivan, J. Tokenized time-series in satellite image segmentation with transformer network for active fire detection. *IEEE Trans. Geosci. Remote Sens.* **2023**, *61*, 4405513. [CrossRef]
10. Chen, J.; Lv, Q.; Wu, S.; Zeng, Y.; Li, M.; Chen, Z.; Zhou, E.; Zheng, W.; Liu, C.; Chen, X.; et al. An adapted hourly Himawari-8 fire product for China: Principle, methodology and verification. *Earth Syst. Sci. Data* **2023**, *15*, 1911–1931. [CrossRef]
11. Xu, H.; Zhang, G.; Chu, R.; Zhang, J.; Yang, Z.; Wu, X.; Xiao, H. Detecting forest fire omission error based on data fusion at subpixel scale. *Int. J. Appl. Earth Obs. Geoinf.* **2024**, *128*, 103737. [CrossRef]
12. Zhang, Q.; Zhu, J.; Dong, Y.; Zhao, E.; Song, M.; Yuan, Q. 10-minute forest early wildfire detection: Fusing multi-type and multi-source information via recursive transformer. *Neurocomputing* **2025**, *616*, 128963. [CrossRef]
13. Hall, J.V.; Schroeder, W.; Rishmawi, K.; Wooster, M.; Schmidt, C.C.; Huang, C.; Csiszar, I.; Giglio, L. Geostationary active fire products validation: GOES-17 ABI, GOES-16 ABI, and Himawari AHI. *Int. J. Remote Sens.* **2023**, *44*, 3174–3193. [CrossRef]
14. Kang, Y.; Sung, T.; Im, J. Toward an adaptable deep-learning model for satellite-based wildfire monitoring with consideration of environmental conditions. *Remote Sens. Environ.* **2023**, *298*, 113814. [CrossRef]
15. Zhang, Q.; Zhu, J.; Huang, Y.; Yuan, Q.; Zhang, L. Beyond being wise after the event: Combining spatial, temporal and spectral information for Himawari-8 early-stage wildfire detection. *Int. J. Appl. Earth Obs. Geoinf.* **2023**, *124*, 103506. [CrossRef]
16. Xu, W.; Wooster, M.J.; He, J.; Zhang, T. Improvements in high-temporal resolution active fire detection and FRP retrieval over the americas using GOES-16 ABI with the geostationary fire thermal anomaly (FTA) algorithm. *Sci. Remote Sens.* **2021**, *3*, 100016. [CrossRef]

17. Hally, B.; Wallace, L.; Reinke, K.; Jones, S.; Skidmore, A. Advances in active fire detection using a multi-temporal method for next-generation geostationary satellite data. *Int. J. Digit. Earth* **2019**, *12*, 1030–1045. [CrossRef]
18. Hally, B.; Wallace, L.; Reinke, K.; Jones, S.; Engel, C.; Skidmore, A. Estimating fire background temperature at a geostationary scale—An evaluation of contextual methods for AHI-8. *Remote Sens.* **2018**, *10*, 1368. [CrossRef]
19. Roberts, G.J.; Wooster, M.J. Fire detection and fire characterization over africa using Meteosat SEVIRI. *IEEE Trans. Geosci. Remote Sens.* **2008**, *46*, 1200–1218. [CrossRef]
20. Giglio, L.; Schroeder, W. A global feasibility assessment of the bi-spectral fire temperature and area retrieval using MODIS data. *Remote Sens. Environ.* **2014**, *152*, 166–173. [CrossRef]
21. Giglio, L.; Schroeder, W.; Justice, C.O. The collection 6 MODIS active fire detection algorithm and fire products. *Remote Sens. Environ.* **2016**, *178*, 31–41. [CrossRef]
22. Schroeder, W.; Prins, E.; Giglio, L.; Csiszar, I.; Schmidt, C.; Morisette, J.; Morton, D. Validation of GOES and MODIS active fire detection products using ASTER and ETM+ data. *Remote Sens. Environ.* **2008**, *112*, 2711–2726. [CrossRef]
23. Hally, B.; Wallace, L.; Reinke, K.; Jones, S. A broad-area method for the diurnal characterisation of upwelling medium wave infrared radiation. *Remote Sens.* **2017**, *9*, 167. [CrossRef]
24. Filizzola, C.; Corrado, R.; Marchese, F.; Mazzeo, G.; Paciello, R.; Pergola, N.; Tramutoli, V. RST-FIRES, an exportable algorithm for early-fire detection and monitoring: Description, implementation, and field validation in the case of the MSG-SEVIRI sensor. *Remote Sens. Environ.* **2016**, *186*, 196–216. [CrossRef]
25. Xu, W.; Wooster, M.J.; Roberts, G.; Freeborn, P. New GOES imager algorithms for cloud and active fire detection and fire radiative power assessment across North, South and Central America. *Remote Sens. Environ.* **2010**, *114*, 1876–1895. [CrossRef]
26. Yan, J.; Qu, J.; Ran, M.; Zhang, F. Himawari-8 AHI fire detection in clear sky based on time-phase change. *Natl. Remote Sens. Bull.* **2020**, *24*, 571–577.
27. Mazzeo, G.; De Santis, F.; Falconieri, A.; Filizzola, C.; Lacava, T.; Lanorte, A.; Marchese, F.; Nolè, G.; Pergola, N.; Pietrapertosa, C.; et al. Integrated satellite system for fire detection and prioritization. *Remote Sens.* **2022**, *14*, 335. [CrossRef]
28. Xu, Y.; Sun, K.; Lv, F.; Bian, Z.; Zhou, X.; Miao, S.; He, T. Identification of severe convective clouds and analysis of their relationship with severe convective weather based on Himawari-8/9 geostationary satellite. *Atmos. Res.* **2026**, *327*, 108349. [CrossRef]
29. Liu, J.; Yu, J.; Lin, C.; He, M.; Liu, H.; Wang, W.; Min, M. Near-real-time atmospheric and oceanic science products of Himawari-8 and Himawari-9 geostationary satellites over the South China Sea. *Earth Syst. Sci. Data* **2024**, *16*, 4949–4969. [CrossRef]
30. Zhuge, X.; Zou, X.; Yu, L.; Li, X.; Zeng, M.; Chen, Y.; Zhang, B.; Yao, B.; Tang, F.; Chen, F.; et al. Introduction to the NJIAS Himawari-8/9 cloud feature dataset for climate and typhoon research. *Earth Syst. Sci. Data* **2024**, *16*, 1747–1769. [CrossRef]
31. Zhang, H.; Sun, L.; Zheng, C.; Ge, S.; Chen, J.; Li, J. A weighted contextual active fire detection algorithm based on Himawari-8 data. *Int. J. Remote Sens.* **2023**, *44*, 2400–2427. [CrossRef]
32. Zhang, D.; Huang, C.; Gu, J.; Hou, J.; Zhang, Y.; Han, W.; Dou, P.; Feng, Y. Real-time wildfire detection algorithm based on VIIRS fire product and Himawari-8 data. *Remote Sens.* **2023**, *15*, 1541. [CrossRef]
33. Zheng, Z.; Hu, H.; Huang, W.; Zhou, F.; Ma, Y.; Liu, Q.; Jiang, L.; Wang, S. Wildfire detection based on the spatiotemporal and spectral features of Himawari-8 data. *IEEE Trans. Geosci. Remote Sens.* **2024**, *62*, 5408213. [CrossRef]
34. Li, F.; Zhang, X.; Kondragunta, S.; Schmidt, C.C.; Holmes, C.D. A preliminary evaluation of GOES-16 active fire product using Landsat-8 and viirs active fire data, and ground-based prescribed fire records. *Remote Sens. Environ.* **2020**, *237*, 111600. [CrossRef]
35. Liu, C.; Chen, R.; He, B. Integrating machine learning and a spatial contextual algorithm to detect wildfire from Himawari-8 data in Southwest China. *Forests* **2023**, *14*, 919. [CrossRef]
36. Wickramasinghe, C.; Wallace, L.; Reinke, K.; Jones, S. Intercomparison of Himawari-8 AHI-FSA with MODIS and VIIRS active fire products. *Int. J. Digit. Earth* **2018**, *13*, 457–473. [CrossRef]
37. Quintano, C.; Fernández-Manso, A.; Fernández-Manso, O. Combination of Landsat and Sentinel-2 MSI data for initial assessing of burn severity. *Int. J. Appl. Earth Obs. Geoinf.* **2018**, *64*, 221–225. [CrossRef]
38. Alcaras, E.; Costantino, D.; Guastaferro, F.; Parente, C.; Pepe, M. Normalized burn ratio plus (NBR+): A new index for Sentinel-2 imagery. *Remote Sens.* **2022**, *14*, 1727. [CrossRef]
39. Miller, J.D.; Thode, A.E. Quantifying burn severity in a heterogeneous landscape with a relative version of the delta normalized burn ratio (DNBR). *Remote Sens. Environ.* **2007**, *109*, 66–80. [CrossRef]
40. Genzano, N.; Filizzola, C.; Paciello, R.; Pergola, N.; Tramutoli, V. Robust satellite techniques (RST) for monitoring earthquake prone areas by satellite TIR observations: The case of 1999 Chi-Chi earthquake (Taiwan). *J. Asian Earth Sci.* **2015**, *114*, 289–298. [CrossRef]
41. Tramutoli, V. Robust Satellite Techniques (RST) for Natural and Environmental Hazards Monitoring and Mitigation: Theory and Applications. In *Proceedings of the 2007 International Workshop on the Analysis of Multi-Temporal Remote Sensing Images, Leuven, Belgium, 18–20 July 2007*; IEEE: New York, NY, USA, 2007; pp. 1–6.
42. Marchese, F.; Filizzola, C.; Genzano, N.; Mazzeo, G.; Pergola, N.; Tramutoli, V. Assessment and improvement of a robust satellite technique (RST) for thermal monitoring of volcanoes. *Remote Sens. Environ.* **2011**, *115*, 1556–1563. [CrossRef]

43. Marchese, F.; Mazzeo, G.; Filizzola, C.; Coviello, I.; Falconieri, A.; Lacava, T.; Paciello, R.; Pergola, N.; Tramutoli, V. Issues and possible improvements in winter fires detection by satellite radiances analysis: Lesson learned in two regions of Northern Italy. *IEEE J. Sel. Top. Appl. Earth Obs. Remote Sens.* **2017**, *10*, 3297–3313. [CrossRef]
44. Lin, Z.; Chen, F.; Niu, Z.; Li, B.; Yu, B.; Jia, H.; Zhang, M. An active fire detection algorithm based on multi-temporal FengYun-3C VIRR data. *Remote Sens. Environ.* **2018**, *211*, 376–387. [CrossRef]
45. Roberts, G.; Wooster, M.J. Development of a multi-temporal Kalman filter approach to geostationary active fire detection & fire radiative power (FRP) estimation. *Remote Sens. Environ.* **2014**, *152*, 392–412.
46. Giglio, L.; Descloitres, J.; Justice, C.O.; Kaufman, Y.J. An enhanced contextual fire detection algorithm for MODIS. *Remote Sens. Environ.* **2003**, *87*, 273–282. [CrossRef]
47. Chen, J.; Yao, Q.; Chen, Z.; Li, M.; Hao, Z.; Liu, C.; Zheng, W.; Xu, M.; Chen, X.; Yang, J.; et al. The Fengyun-3D (FY-3D) global active fire product: Principle, methodology and validation. *Earth Syst. Sci. Data* **2022**, *14*, 3489–3508. [CrossRef]
48. Schroeder, W.; Oliva, P.; Giglio, L.; Csiszar, I.A. The new VIIRS 375 m active fire detection data product: Algorithm description and initial assessment. *Remote Sens. Environ.* **2014**, *143*, 85–96. [CrossRef]
49. Zhang, N.; Sun, L.; Sun, Z.; Qu, Y. Detecting low-intensity fires in east Asia using VIIRS data: An improved contextual algorithm. *Remote Sens.* **2021**, *13*, 4226. [CrossRef]
50. Scaduto, E.; Chen, B.; Jin, Y. Satellite-based fire progression mapping: A comprehensive assessment for large fires in Northern California. *IEEE J. Sel. Top. Appl. Earth Obs. Remote Sens.* **2020**, *13*, 5102–5114. [CrossRef]

Disclaimer/Publisher's Note: The statements, opinions and data contained in all publications are solely those of the individual author(s) and contributor(s) and not of MDPI and/or the editor(s). MDPI and/or the editor(s) disclaim responsibility for any injury to people or property resulting from any ideas, methods, instructions or products referred to in the content.